Benchmarking a DEM-CFD Model of an Optical Belt Sorter by Experimental Comparison

Albert Bauer[1],*, Georg Maier[2], Marcel Reith-Braun[3], Harald Kruggel-Emden[1], Florian Pfaff[3], Robin Gruna[2], Uwe Hanebeck[3], and Thomas Längle[2]

Dedicated to Prof. Dr.-Ing. Joachim Werther on the occasion of his 80th birthday

A DEM-CFD (discrete element method – computational fluid dynamics) model of an optical belt sorter was extensively compared with experiments of a laboratory-scale sorter to assess the model's accuracy. Brick and sand-lime brick were considered as materials. First, the transport characteristics on the conveyor belt, involving mass flow, lateral particle distribution and proximity, were compared. Second, sorting results were benchmarked for varying mixture proportions at differing mass flows. It was found that the numerical model is able to reproduce the experimental results with high accuracy.

1 Introduction

With the continuous increase in computational power, simulations of natural and technical processes have become more and more widespread in the last decades. Particularly for systems that involve large amounts of particles, which are usually found in the fields of geoscience, civil and process engineering, the discrete element method (DEM) showed to be valuable for a wide range of applications. In the DEM, each particle is modeled discreetly. The interaction between particles as well as particles and walls over time is then computed by using contact modeling incorporating physical properties, with parameters typically obtained by calibration experiments.

The DEM can address dynamic problems involving large and complex geometries due to the absence of mesh discretization. Transport processes [1] of rock material [2,3] and granular matter or powder flow in mixers, drums or hoppers are simulated with the DEM [4,5]. Coupling to other simulation methods is also feasible to extend the investigable fields. In particular, coupling with the finite element method (FEM) [6,7] or computational fluid dynamics (CFD) [8–10] is commonly used to investigate multiphysics processes, involving mechanical/thermomechanical phenomena at particles or particle/fluid interaction. Challenges up to now of DEM simulations are the treatment of vast particle amounts of more than 10^8, the consideration of highly irregularly shaped particles and the calibration procedure itself [5].

For this study, the DEM-CFD method was applied to model an optical belt sorter. Optical belt sorting belongs to the field of sensor-based sorting, where a bulk material is separated based upon its physical properties. The general work principle can be summarized as follows. The material is fed on a conveyor belt, where it is transported towards a sensor, which measures certain properties. After discharge from the conveyor belt, the sorting step is applied at which the material is separated into at least two fractions based on the identified properties. Properties of the material to be sorted may be optical properties or other physical properties. The separation can be realized for example mechanically or by magnets, eddy currents as well as air jets. An extensive overview of sensor-based sorting of municipal waste, which is also one of the most prominent applications, is given in [11]. Further applications are in food processing [12–14], minerals processing [15–17], and sorting of construction and demolition waste (C&DW) [18, 19].

[1]Albert Bauer   https://orcid.org/0000-0002-7906-4036, Harald Kruggel-Emden
(a.bauer@tu-berlin.de)
Technische Universität Berlin, Chair of Mechanical Process Engineering and Solids Processing, Ernst-Reuter-Platz 1, 10587 Berlin, Germany.

[2]Georg Maier, Robin Gruna, Thomas Längle
Fraunhofer IOSB, Institute of Optronics, System Technologies and Image Exploitation, Fraunhoferstraße 1, 76131 Karlsruhe, Germany.

[3]Marcel Reith-Braun, Florian Pfaff, Uwe Hanebeck
Intelligent Sensor-Actuator-Systems Laboratory (ISAS), Karlsruhe Institute of Technology, Adenauerring 2, 76131 Karlsruhe, Germany.

Our research was motivated by the goal to model the entire sorting process of an optical belt sorter. A precise simulation model would not only open new possibilities regarding the optimization of the sorting process and drastically decrease the amount of labor and cost intensive experimental work but would also allow the investigation of the sorting process of potentially harmful substances, such as hazardous substances in C&DW. For this purpose, a laboratory-scale optical belt sorter was modeled with a DEM-CFD approach. A rubble bulk material consisting of brick and sand-lime brick was considered. The two materials were discriminated by their color and ejected using pneumatic separation. The particles and the walls were simulated by the DEM, the air jets were simulated by the CFD. Both phases were coupled in the region where particles are deflected by air jets. For a more comprehensive understanding of the analyzed sorting system, the transport and the sorting phase were investigated separately in the simulations and the experiments.

Only few studies exist concerning research on the numerical investigation of optical belt sorting. In [20], the authors used a Monte-Carlo simulation method to investigate the feed characteristics of an automated sorter. In [21], a DEM-CFD framework was utilized to investigate the particle ejection of flat and cubic particles in a simplified sorting step involving a single valve. The transport of a bulk of spheres, cylinders, and plates on an automated sorter was compared with experiments in [22]. A MATLAB model was used to assess the influence of belt length and other parameters on the sorting efficiency. In [23], the authors numerically studied the influence of the sorting algorithm and several other parameters on the sorting accuracy of an optical belt sorter with a DEM-CFD approach. Exiting mass flows at the feeder and sorting results at one input composition were also experimentally compared.

Regarding the aforementioned publications, the contributions of this work can be summarized as follows. An extensive comparison of transport and sorting characteristics for various input feed conditions is conducted for the first time. Also, the complexity of our modeling approach is increased in two ways compared to preceding work. Firstly, a real bulk material is considered in the DEM-CFD. Secondly, the computation of the number and duration of active fluid jets is performed identically to the experimental system. Finally, the possibility to model a full sorting system with accurate results by utilizing the DEM-CFD is proven.

The article is divided into five sections. In Sect. 2, the sorting task, setup and numerical model are introduced. In Sect. 3, the investigation procedure is outlined. The results of the transport and sorting experiments and simulations are presented and discussed in Sect. 4. Lastly, conclusions are drawn in Sect. 5.

## 2 Setup and Methods

2.1 Sorting Task and Belt Sorter Setup

As a sorting task, we chose a sorting scenario from the field of C&DW. We consider a binary mixture of brick and sand-lime brick, as shown in Fig. 1. The densities of the materials were $2541\,kg\,m^{-3}$ for brick and $2565\,kg\,m^{-3}$ for sand-lime brick with a size range of 4–8 mm determined by sieving analysis. The laboratory-scale sorting system is shown in Fig. 2a. Its model replicate is outlined in Fig. 2b.

Figure 1. Mixture of bulk material to be sorted. Brick (orange) and sand-lime brick (grey).

Both brick and sand-lime brick are fed into the system by a combination of a silo and an electromagnetic feeder (see Fig. 2a) that operates at a constant frequency of 50 Hz. The amplitude is adjustable and used to steer the intended mass flow. The lower feeder is used to transport sand-lime brick, the upper feeder is transporting brick. From the feeders, the materials are mixed and pre-accelerated via a chute onto a conveyor belt. The conveyor belt has a length of 600 mm and a width of 140 mm. The system is equipped with a color line-scan camera (not shown in Fig. 2a). This inspection camera observes the material 25 mm after being discharged from the belt. The line width of the camera model used is 1365 pixel and the maximum line frequency is 14.8 kHz. In the course of this study, the mixed material is sorted based on the color. Additional to this inspection camera, the system is equipped with an area-scan camera (shown in Fig. 2a). This camera is used to observe the material on the conveyor belt to evaluate the particle positions. It is not used as an inspection camera for the calculation of sorting decisions in this study. The area-scan camera has a CMOS sensor with global shutter and offers 2320×1726 pixel at a maximum frame rate of 192 Hz. Note that no cameras (area-scan, line-scan) are foreseen in the numerical model of the optical belt sorter (Fig. 2b) as colors, positions and velocities of particles are fully accessible over time.

Material separation is carried out by means of a series of pneumatic fast-switching valves, which activate related nozzles (see Fig. 2a). The nozzle bar is equipped with
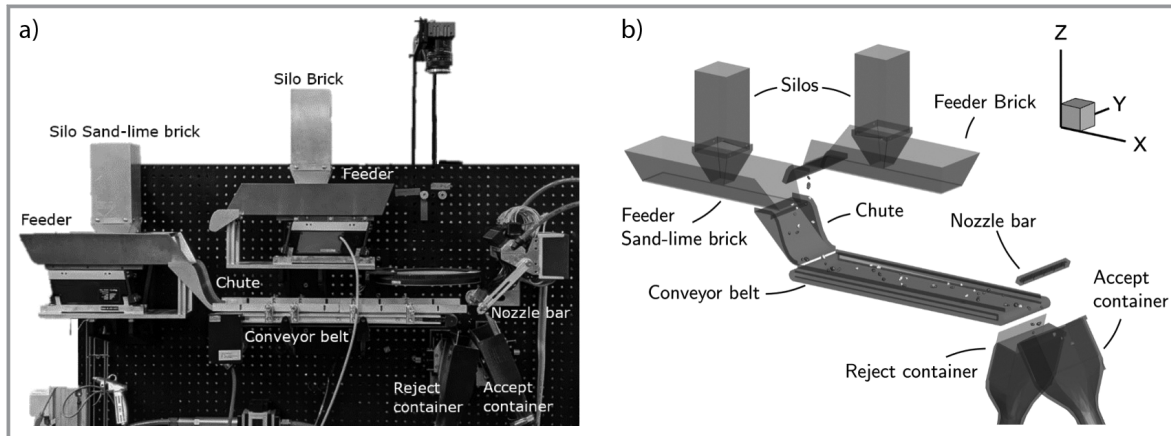
Figure 2. a) Experimental setup of the optical belt sorter. In this photo, only the area-scan camera used to observe the material on the conveyor belt is shown. b) Numerical model of the optical belt sorter.

32 nozzles in total. Besides the classification of individual particles, the control signals for material separation are calculated based on an image processing algorithm. A so-called deflection window is obtained. It describes the duration and point in time for the deflection of a single particle. The extent of the window perpendicular to the transport direction is based on the extend of the particle in this direction and determines which valves are opened. Alike, the opening duration of the valves is based on the extend of the particle in transport direction. By assuming the particle velocity to be equal to the belt velocity, a fixed time delay is used to compute the point in time for valve activation, including the activation delay of the valves themselves. It is further assumed that there exists no velocity of the particles crosswise to the transport direction.

Additionally, a system for the online assessment of the sorting quality during an experiment was implemented. The resulting setup is shown in terms of a CAD drawing in Fig. 3. It consists of two chutes, onto which the fractions of the reject and accept containers are fed. A line-scan camera is used to record both material streams and classify individual particles. Using this information, time resolved statistics regarding the ratio of the materials can be calculated for both sorting fractions, such as the true positive rate and true negative rate, see Sect. 3.2.
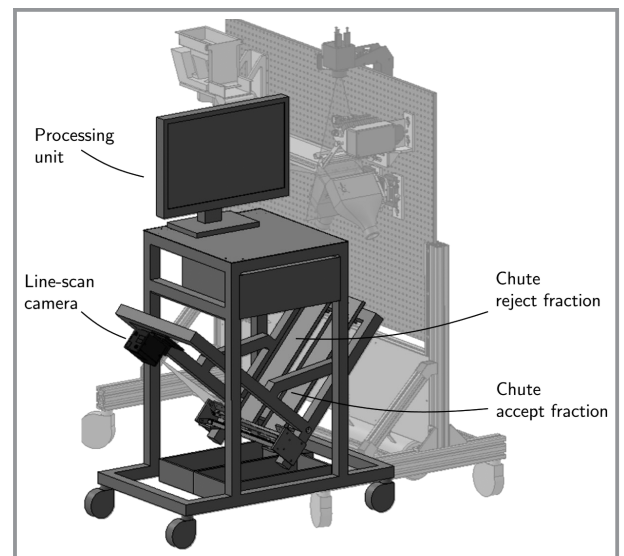
2.2 Numerical Model

2.2.1 Governing Equations of the DEM-CFD

Mostly adapting the DEM-CFD approach of [23], force equilibrium yields

$$\ddot{\vec{x}_i}\, m_i = \overrightarrow{F_i^c} + \overrightarrow{F_i^g} + \overrightarrow{F_i^f} \tag{1}$$

where the acceleration $\ddot{\vec{x}_i}$ of particle i with mass m_i is caused by acting forces on that particle: $\overrightarrow{F_i^c}$ is the summed

Figure 3. CAD drawing of the resulting setup for online assessment of the time resolved sorting quality.

contact force originating from contact with other particles and walls, $\overrightarrow{F_i^g}$ is the gravitational force and $\overrightarrow{F_i^f}$ is the force caused by interaction with the surrounding fluid. Rotational motion is given by

$$J_i\, \dot{\overrightarrow{\omega_i}} + \overrightarrow{\omega_i} \times \left(J_i \overrightarrow{\omega_i} \right) = \Lambda_i^{-1}\, \overrightarrow{T_i^c} \tag{2}$$

where $\overrightarrow{T_i^c}$ is the summed torques induced by wall and particle interactions through sliding friction and $\overrightarrow{T_i^r}$ by rolling friction. No torques are induced by fluid interaction. J_i is the mass tensor of inertia given in the principal axes, $\dot{\overrightarrow{\omega_i}}$ denotes the angular acceleration in the body fixed frame, $\overrightarrow{\omega_i}$ represents the angular velocity in the body fixed frame and Λ_i^{-1} is the rotation matrix converting a vector from the inertial into the body fixed frame. The contact forces were mod-

eled by a linear spring-dashpot model. For computation, each force was split into a normal and a tangential component. Both components yield $\overrightarrow{F^n} = k^n \delta \vec{n} + \gamma^n \vec{v}_{rel}^n$ and $\overrightarrow{F^t} = \min\left(k^t \left|\overrightarrow{\xi^t}\right|, \mu_c \left|\overrightarrow{F^n}\right|\right)\vec{t}$ for the normal and tangential force, respectively. Superscripts n and t denote normal and tangential components, respectively. k^n is the normal spring stiffness, δ the virtual overlap, $\vec{n}$ the normal vector, γ^n the normal damping coefficient and $\vec{v}_{rel}^n$ the relative velocity in normal direction at the contact point. k^t is the tangential spring stiffness, $\overrightarrow{\xi^t}$ is the tangential displacement, μ_c is the coefficient of Coulomb friction and $\vec{t}$ is the tangential vector. The rolling friction model [24] was adapted, which yields $\overrightarrow{T_i^r} = -\mu_r \left|\overrightarrow{F^n}\right| R_r \frac{\overrightarrow{\omega_{rel}}}{\left|\overrightarrow{\omega_{rel}}\right|}$, with rolling friction μ_r, the rolling radius R_r and the relative angular velocity $\overrightarrow{\omega_{rel}}$ between two contacting particles.

The fluid phase which is present in the area of the nozzle jets is described by conservation of mass (Eq. (3))

$$\frac{\partial \rho_f}{\partial t} + \nabla\left(\rho_f \vec{u}\right) = 0 \tag{3}$$

and conservation of momentum (Eq. (4)), respectively

$$\frac{\partial\left(\rho_f \vec{u}\right)}{\partial t} + \nabla\left(\rho_f \vec{u}\,\vec{u}\right) = -\nabla p + \nabla \tau + \rho_f \vec{g} \tag{4}$$

In Eqs. (3) and (4) ρ_f is the fluid density, $\vec{u}$ the fluid velocity, p the pressure, $\vec{g}$ the gravitational acceleration and τ the stress tensor. For turbulence modeling, we use the Reynolds-averaged Navier-Stokes equations, so that the stress tensor can be written as

$$\tau = \eta_e \left[(\nabla \vec{u}) + (\nabla \vec{u})^{-1}\right] \tag{5}$$

where η_e is the effective viscosity which is obtained through turbulence modeling. For calculation of the fluid force $\overrightarrow{F_i^f}$ on the particles in Eq. (1) in the coupling region, the drag model of [25] was utilized. It is applicable to non-spherical particle shapes and calculated by

$$\overrightarrow{F_i^f} = \overrightarrow{F_i^d} + \overrightarrow{F_i^{\nabla p}} = \frac{1}{2}\rho_f |\vec{u} - \vec{v}| c_D A_\perp \varepsilon_f^{1-\chi}(\vec{u} - \vec{v}) \tag{6}$$

The fluid force is the sum of drag $\overrightarrow{F_i^d}$ and pressure gradient force $\overrightarrow{F_i^{\nabla p}}$. Velocities of fluid and particles are denoted by $\vec{u}$ and $\vec{v}$, respectively. c_D denotes the drag coefficient of a particle, $A_\perp$ the projection area perpendicular to the flow direction, ρ_f the fluid density and ε_f is the local voidage. It holds that $0 < \varepsilon_f < 1$ due to the solid phase in the fluid. χ is an empirical correction factor and depends on the particle Reynolds-number Re They are given by

$$\chi = 3.7 - 0.65 \exp\left(-\frac{(1.5 - \log(Re))^2}{2}\right) \tag{7}$$

and

$$Re = \frac{1}{\eta_f}\varepsilon_f \rho_f d_p |\vec{u} - \vec{v}| \tag{8}$$

The drag coefficient c_D of the individual particle was computed by the correlation of [26], which yields

$$C_D = \frac{8}{Re}\frac{1}{\sqrt{\phi_\perp}} + \frac{16}{Re}\frac{1}{\sqrt{\phi}} + \frac{3}{\sqrt{Re}}\frac{1}{\phi^{3/4}}$$
$$+ 0.42 \times 10^{0.4(-\log(\phi))^{0.2}}\frac{1}{\phi_\perp} \tag{9}$$

To our knowledge, the drag correlation is the most accurate formulation for arbitrary particle shapes, since it takes the particle shape into account by using the crosswise sphericity $\phi_\perp$. Note that the fluid flow around the individual particles was not resolved. A one-way coupling strategy was used to model the particle-fluid interaction. The fluid fields were computed once and were then coupled to the DEM-CFD each time a particle reached the area of the nozzles. Hence, the particle was influenced by the fluid field, but not vice versa.

2.2.2 Representation of the Nozzle Bar Fluid Field

The preparation of the fluid field to be used in the DEM-CFD resulting from individual nozzle activation required several steps. First, the fluid field of a single nozzle was simulated with the CFD software Ansys Fluent based on the available CAD data of the nozzle (details not given here). We used a stationary RANS simulation with a k-ε turbulence model, which is well suited for free stream phenomena [27]. The pressure difference between nozzle inlet and ambient room was set at 0.75 bar. Second, the fine CFD mesh with about 6.5 million cells was coarsened to about 10 000 cells. Third, the field of the single nozzle was concatenated 32 times to form the full fluid field of the nozzle bar.

2.2.3 Particle Model and Contact Parameters

To model both materials as part of the DEM-CFD exemplary particle shapes were obtained by tomographic reconstruction (13 sand-lime brick particles and 11 brick particles). The obtained shapes were then approximated by a certain number of clustered spheres per particle (15–20 spheres). For each exemplary particle shape the genetic algorithm of MATLAB was utilized to reduce the difference between the volume of the tomographically obtained shape and the volume of the clustered spheres. A resulting exemplary cluster particle is shown in Fig. 4a. A major advantage of clustered particles is that complex shapes can be approximated while computing time and complexity of contact detection remains relatively low. The principle of a cluster particle contact is shown in Fig. 4 b for the collision of two exemplary particles, A and B. Utilizing a linear spring-dash-
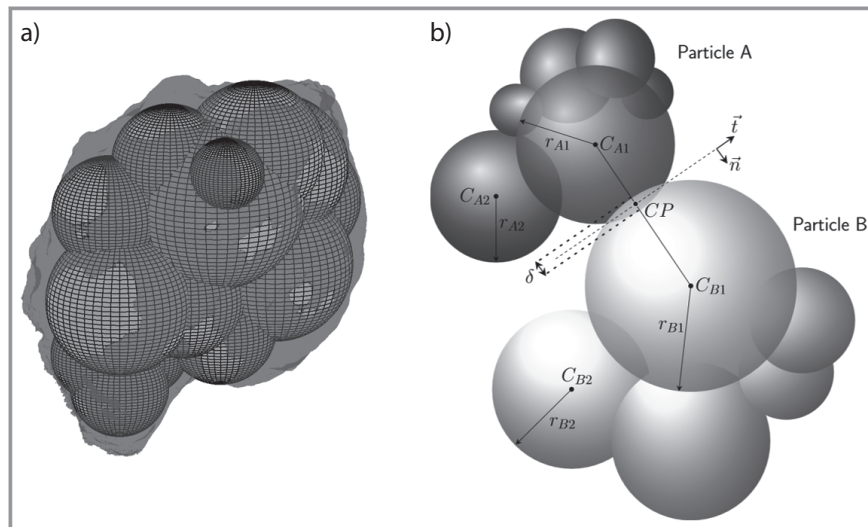
Figure 4. Exemplary cluster particle in the hull to be approximated (a). Relevant quantities for cluster particle collision (b).

pot model (see Sect. 2.2.1) leads to an overlap δ between the respective contacting subspheres with centroids C_{A1} and C_{B1}. As particles comprise of subspheres, contact detection of clustered sphere particles is analogue to contact detection of individual spherical particles. Contact force models as for spheres can be used (see Sect. 2.2.1). Only the integration of rotational motion is more complex as Eq. (2) has to be solved instead of just $J_i\ \vec{\omega}_i = \overrightarrow{T_i^c} + \overrightarrow{T_i^r}$, as it is the case for spheres.

As a next step after addressing the particle approximation, sliding friction, rolling friction and coefficient of restitution (COR) were calibrated for all possible material pairs analogous to [28]. Small scale laboratory experiments were conducted and simulated. The parameters of interest were varied until the results of experiments and simulations matched. Static angle of repose, dynamic angle of repose and a plate impact experiment were performed to obtain the desired parameter sets for brick and sand-lime brick which can get in contact with itself, each other or wall materials made of rubber (conveyor belt) or steel (sorter walls). Tab. 1 summarizes the calibrated parameters. Note that all obtained contact parameters can either be directly applied in the DEM-CFD or in case of the COR be used to calculate a corresponding normal stiffness k^n and a damping coefficient γ^n. The tangential stiffness k^t is calculated based on mechanical material properties (Poisson's ratio and Young's modulus).

2.2.4 Modeling of the Vibrating Feeder Plates

To model the vibrating feeder plates, the vibration amplitudes in all three directions were measured at all four corners of both material feeders described in Sect. 2.1 with a 3D accelerometer. Due to lack of accessibility, the vibration could not be measured at the center of the plates. The time signals were transformed into phase averaged periods by utilizing a Hilbert-transformation, yielding the instantane-

ous phase and amplitude of a signal [29]. The phase averaged amplitudes showed a clear dependency on the accelerometer position. While the difference between the back and the front region of the feeder is a desired behavior to transport the bulk to the front, the disbalance between the amplitudes of the left and right side of a feeder is unwanted. Furthermore, both feeders behaved differently. To approximate the vibration pattern of the plates, a linear interpolation of the amplitude between the four measured corners was used for the simulations. Each contact point between a particle and the plate was evaluated by weighting the proximity to each plate corner, where the amplitude was known.

Table 1. Calibrated mechanical parameters of both materials with all contact partners. (P) refers to the contacting particle either sand-lime brick or brick which gets in contact with either sand-lime brick (SB), brick (B), conveyor belt (CB) or sorter wall (SW) material.

Material	Sand-lime brick	Brick
COR P-SB [–]	0.19	0.215
COR P-B [–]	0.215	0.24
COR P-CB [–]	0.19	0.1
COR P-SW [–]	0.19	0.1
Sliding friction P-SB [–]	0.19	0.18
Sliding friction P-B [–]	0.18	0.17
Sliding friction P-CB [–]	0.4	0.56
Sliding friction P-SW [–]	0.4	0.56
Rolling friction P-SB [–]	$2 \cdot 10^{-2}$	$1.2 \cdot 10^{-2}$
Rolling friction P-B [–]	$1.2 \cdot 10^{-2}$	$3.8 \cdot 10^{-3}$
Rolling friction P-CB [–]	$7.5 \cdot 10^{-3}$	$5.8 \cdot 10^{-3}$
Rolling friction P-SW [–]	$7.5 \cdot 10^{-3}$	$5.8 \cdot 10^{-3}$

3 Investigation Procedure

For a comprehensive benchmarking of the capabilities of the sorter model with respect to experiments, the analysis of the sorting process was divided into two steps. First, material transport investigations with a pure bulk material were conducted both experimentally and numerically without performing sorting. Thereby, a critical evaluation of the particle model, the DEM contact representation and the model of the vibrating feeder plates was feasible. Second, sorting investigations with premixed material were carried out. This way, both

stages of the sorting process could be analyzed separately. Additionally, potential errors in the simulated material feed did not affect the sorting results in the simulations.

3.1 Bulk Transport Analysis

In the material transport investigations, each silo (brick, sand-lime brick) was half filled both in the experiments and the numerical investigations. After being transported onto the conveyor belt, each material was captured individually by the area-scan camera towards the end of the conveyor belt in the experiments. The same observation window was applied in the simulations where particle positions were known. The observation window had a length of 10 cm in transport direction and was aligned with the end of the conveyor belt. For both materials, it was recorded:

1) mass flows intended to be $10\,\mathrm{g\,s^{-1}}$, $15\,\mathrm{g\,s^{-1}}$, $20\,\mathrm{g\,s^{-1}}$ by applying the amplitudes from the experiments,
2) lateral distribution on the conveyor belt,
3) average closest distance to neighbor particles.

As the first step of comparison, it was assessed if the simulated mass flows coincided with the experimental mass flows. As a next step, the lateral particle position was evaluated along a fixed line in y-direction (see coordinate system in Fig. 2b). The line of evaluation was set 5 cm ahead of the end of the conveyor belt. Another spatial quantity was given by analyzing the average minimal particle distance. It was calculated by

$$\frac{\sum_{i=1}^{n} \min\left(|\vec{x}_i - \vec{x}_j|\right)}{n} \tag{10}$$

with $I \neq j$ and j running from 1 to n neighbor particles as observed in the observation window in each camera frame and simulation time step.

3.2 Sorting Investigations

The second part of the benchmark focused on the sorting step. To compare experimental and numerical efficiency at several operating conditions, three compositions of material were sorted at two mass flows. Proportions of 90:10, 75:25 and 50:50 were processed at $10\,\mathrm{g\,s^{-1}}$ and $20\,\mathrm{g\,s^{-1}}$. The first percentage denotes the accept material, i.e., sand-lime brick, and the second percentage denotes the reject material, i.e., brick. Each investigation in both experiment and simulation covered a sorting duration of 60 s.

The true positive rate and true negative rate were computed to measure the sorting accuracy. They were defined as

$$\mathrm{TNR} = \frac{\text{True negatives}}{\text{True negatives} + \text{False positives}} \tag{11}$$

$$\mathrm{TPR} = \frac{\text{True positives}}{\text{True positives} + \text{False negatives}} \tag{12}$$

and denote the rates of correctly sorted reject and accept material, respectively. To decouple possible uncertainties in material feed, the feed of both vibration feeders was replaced with a mass flow inlet of premixed material above the chute in the simulations. In the experimental system, the feeder of sand-lime brick was used to transport a manually premixed bulk material onto the chute.

4 Results

In the following, the results of the benchmarking are presented starting with the bulk transport and followed by the sorting. In the figures a fixed shade was assigned to each analyzed mass flow: $10\,\mathrm{g\,s^{-1}}$ is depicted white, $15\,\mathrm{g\,s^{-1}}$ is colored bright grey and $20\,\mathrm{g\,s^{-1}}$ is colored dark grey.

4.1 Comparison of Bulk Transport

The evaluated mass flows are shown in Fig. 5 a for sand-lime brick and in b for brick. The values are averaged over 30 s of experimental and simulation time. Continuous lines indicate experimental results and dashed lines show numerical data.

For sand-lime brick at intended $10\,\mathrm{g\,s^{-1}}$, the experimental mass flow of $9.6\,\mathrm{g\,s^{-1}}$ is clearly overestimated by the simulation, which reports $13.2\,\mathrm{g\,s^{-1}}$ (24.2 % deviation). This discrepancy decreases at the higher mass flows, where the deviations are $0.6\,\mathrm{g\,s^{-1}}$ (4 %) at intended $15\,\mathrm{g\,s^{-1}}$ and $1.2\,\mathrm{g\,s^{-1}}$ (6 %) at intended $20\,\mathrm{g\,s^{-1}}$. The mass flow rates of brick show better agreement between simulation and experiment. The most prominent discrepancy of $0.6\,\mathrm{g\,s^{-1}}$ is found at intended $15\,\mathrm{g\,s^{-1}}$. The other mass flows coincide with a deviation of less than 1 %.

Fig. 6 summarizes the results of the lateral particle distribution. Particles along a line orthogonal to the transport
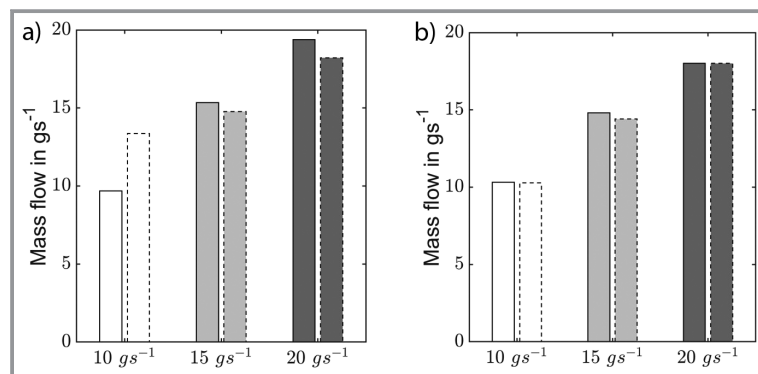
Figure 5. Comparison of experimental (continuous lines) and numerical (dashed lines) mass flows for both bulk materials. Sand-lime brick is shown in (a), brick in (b). Values are averaged over 30 s.
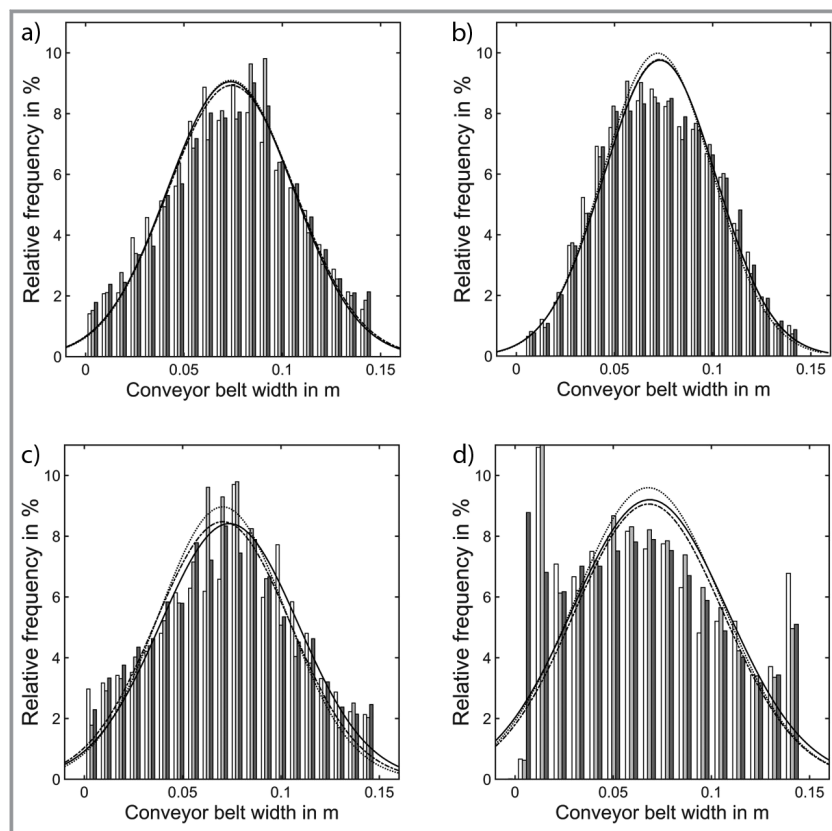
Figure 6. Relative frequency of lateral particle distribution orthogonal to transport direction. Experimental data of sand-lime brick is shown in (a), numerical data in (b). Experimental data of brick is shown in (c), numerical data in (d).

direction were counted and evaluated in histograms with 20 bins. Experimental data is shown in (a) and (c), numerical data is presented in (b) and (d). The histograms show the relative frequency of particle presence along the width of the conveyor belt. Additionally, all histograms were fitted with a normal distribution.

The simulated transport of sand-lime brick coincides well with the experiment, cf. Fig. 6a and 6b. Both plots show relative frequencies of around 8 % at the center, which decline at the rate of a normal distribution. The distribution in the simulation is slightly narrower than in the experiment and nearly identical for all mass flows.

The histogram of brick in the experiment shows to follow almost a normal distribution, comp. Fig. 6c. Around 8 % of the particles move near the center of the conveyor belt. The relative frequency declines towards the edges of the belt. There is only minor difference between the mass flows. For the simulation, the distribution of particles is broader and not symmetric, see Fig. 6 d. On the left side of the conveyor belt, around 50 % more material is being transported than on the right side. There are also notable peaks at both edges of the conveyor belt. While the trans-

port at the center of the belt is predicted accurately by the numerical model, it shows clear deviations towards the edges of the belt. A cause may be the vibration amplitudes at the corners of the feeder for brick, which differ much less than at the feeder of sand-lime brick. As a consequence, the resulting particle distribution is broader and interaction with the conveyor belt side walls may occur resulting in the distribution as seen in Fig. 6d.

In Fig. 7a, the average minimal distances of sand-lime brick particles are presented for experiment and simulation. The average minimal distance is around 3 cm at intended $10\,g\,s^{-1}$ and decreases slightly with increasing mass flow. The distances in the simulations decrease analogously but are around 0.15 cm higher (5 % deviation). A cause could be the slightly higher mass flows in the simulation. Similar trends can be observed for the averaged minimal distances of brick particles, depicted in Fig. 7b. In the simulation, the distances of the brick particles are slightly overestimated, with the highest deviation of 0.37 cm at preset $20\,g\,s^{-1}$ (11.4 %). At the other mass flows, the discrepancy is 0.05 cm (1.5 %) and 0.2 cm (5 %).

To conclude on the bulk transport, there is good agreement between experiment and simulation with accordance of 95 % or above in most cases. However, for some quantities the errors are around 20 %. More data of the vibration amplitudes of the feeders would be beneficial to improve the modeling approach.
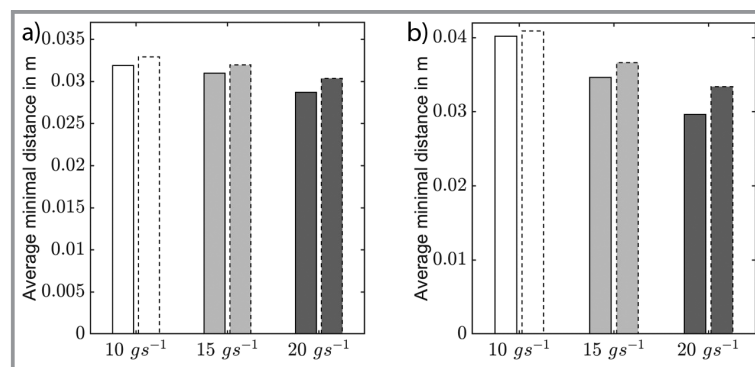
Figure 7. Comparison of average minimal particle distance on the conveyor belt. Sand-lime brick is shown in (a), brick in (b). Experimental data is indicated with continuous lines, numerical data with dashed lines.
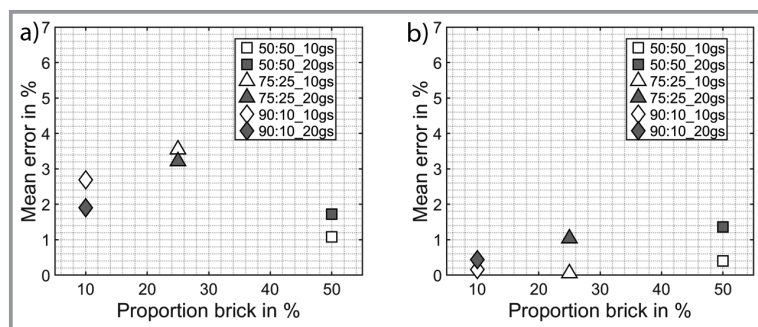
4.2 Comparison of Sorting

In the second part of the comparison, sorting experiments and simulations were performed. As described in Sect. 3.2, the sorting results were compared for six different scenarios. All scenarios were evaluated in terms of the TNR and TPR, see Eqs. (11) and (12). The TNR denotes the rate of correctly sorted particles, the TPR denotes the rate of correctly not separated particles. Fig. 8a and b present the deviation of the TNR and TPR between experiment and simulation for all scenarios. As before, scenarios with a mass flow of $10\,g\,s^{-1}$ are depicted in white, $20\,g\,s^{-1}$ are depicted dark grey. The proportion of brick, which was sorted out, is given by the second number of the proportion and is also the parameter on the x-axis in Fig. 8. As for the TNR in Fig. 8a, the highest errors of 3.5 % are observed at a 75:25 mixture. The errors of the other two mixtures are 3 % for 90:10 and 1.8 % for 50:50. The TPR in Fig. 8b shows similar results. The mean error has a maximum value of 1.4 % at 50:50 and $20\,g\,s^{-1}$. There is only minor difference in TNR and TPR, if the mass flow is changed.

Absolute values of both TNR and TPR are shown in Tab. 2. The TNR is around 97 % for all scenarios and shows a slight tendency to decrease with an increasing proportion of brick. The TPR is above 99 % at all sorting scenarios. Here, a clear tendency is not visible.

Table 2. Values of TNR and TPR in % of sorting experiments and simulations. Experiments were carried out three times and averaged for each input configuration.

Scenario	TNR [%]		TPR [%]	
	Experiment	Simulation	Experiment	Simulation
$90{:}10 - 10\,g\,s^{-1}$	97.68	95.12	99.83	99.67
$90{:}10 - 20\,g\,s^{-1}$	96.85	98.73	99.75	99.32
$75{:}25 - 10\,g\,s^{-1}$	94.78	98.27	99.38	99.43
$75{:}25 - 20\,g\,s^{-1}$	95.13	98.29	99.60	99.58
$50{:}50 - 10\,g\,s^{-1}$	96.11	97.15	99.44	99.05
$50{:}50 - 20\,g\,s^{-1}$	95.45	97.12	99.32	97.98

Figure 8. Comparison of sorting results at three input proportions and two mass flows. (a) shows the correctly deflected particles (TNR) and (b) the correctly not-deflected particles (TPR).

To conclude on the sorting, with maximal errors of 3.5 %, the sorter model proved to yield very good agreement with the experiments. A broad range of input compositions at two distinct mass flows showed to be reproduced well by the simulations, independently of the scenario.

5 Conclusions

In this study, a DEM-CFD model was utilized to model a laboratory-scale optical belt sorter. The experimental sorting system was used to benchmark the numerical model for various scenarios. C&DW waste consisting of brick and sand-lime brick was considered to conduct the experiments. The particles of differing shapes and sizes were approximated with multi-sphere clusters.

In the first part of the investigation, the focus was on the vibrating feeders and the transport behavior was assessed on the conveyor belt for each material separately. Mass flows, lateral particle distributions and minimal average particle distances were compared. The numerical results showed good agreement with the experimental data, but a few larger deviations were also observed. Those arose most likely from the complex vibration pattern of the feeder. In the second part of the investigation, the sorting results were compared in terms of the TNR and TPR. At all investigated inflow conditions, there was high agreement between experiment and simulation. To sum up, it was shown that the applied approach to numerically model a full optical sorting system is suitable to reproduce experimental results. Furthermore, it was demonstrated that computation of ejection windows and nozzle numbers analogous to the experimental system yielded precise sorting results.

Similar numerical simulations could be used to predict the behavior of complex industry-scale sorting machines in the future. With the possibility to track particle movements and interaction with other components, for example with the fluid jets, numerical optimization of such processes becomes much more feasible. Further investigations could include data of various operational points, such as higher mass flows of the bulk material. Particle trajectories could be analyzed during the flight phase to optimize the sorting step. Compared to experimental investigation, a numerical model reduces time consumption and cost of development drastically. Moreover, experimentally difficult to handle scenarios such as sorter operation near its limit or sorting of potentially harmful materials can be studied. However, a correct set up of numerical models remains challenging, as the vibrating feeder plate has shown. Each component introduces additional uncertainties into the system and must be treated with caution. If possible, an isolated investigation of each component is reasonable before considering an entire system.

Symbols used

A	[m^2]	projecton area
C	[–]	coefficient
C	[–]	centroid
$\vec{F}$	[N]	force vector
J	[kg m^2]	mass inertia tensor
k	[N m^{-1}]	spring stiffness
m	[kg]	mass
$\vec{n}$	[–]	normal vector
n	[–]	particle number
r	[m]	radius
R	[m]	radius
Re	[–]	Reynolds number
$\vec{T}$	[N m]	torque vector
t	[s]	time
$\vec{t}$	[–]	tangential vector
$\vec{u}$	[m s^{-1}]	fluid velocity vector
$\vec{v}$	[m s^{-1}]	particle velocity vector
$\vec{x}$	[m]	particle position vector

Greek letters

γ	[kg s^{-1}]	damping coefficient
δ	[m]	overlap
ε	[–]	local voidage
η	[N s m^{-2}]	dynamic fluid viscosity
μ	[–]	friction coefficient
$\vec{\xi}$	[m]	displacement vector
ρ	[kg m^{-3}]	density
τ	[N m^{-2}]	stress tensor
ϕ	[–]	sphericity
χ	[–]	correction factor
$\vec{\omega}$	[s^{-1}]	angular velocity vector
Λ_i^{-1}	[–]	rotation matrix

Sub- and Superscripts

A	particle A
B	particle B
c	Coulomb
c	contact
d	drag
D	drag
e	effective
f	fluid
g	gravitation
i	particle index
j	particle index
n	normal
p	pressure
r	rolling
rel	relative
t	tangential
$\cdot$	temporal derivation
$\perp$	perpendicular to flow direction

Abbreviations

B	brick
CB	conveyor belt material
C&DW	construction and demolition waste
CFD	computational fluid dynamics
CP	contact point
DEM	discrete element method
FEM	finite element method
SB	sand-lime brick
SW	sorter wall material
TNR	true negative rate
TPR	true positive rate

References

[1] D. Gelnar, J. Zegzulka, *Discrete Element Method in the Design of Transport Systems: Verification and Validation of 3D Models*, Springer International Publishing, Cham, **2019**. DOI: https://doi.org/10.1007/978-3-030-05713-8

[2] D. Barreto, J. Leak, in *Modeling in Geotechnical Engineering*, Elsevier, Edinburgh, **2021**, 79–100. DOI: https://doi.org/10.1016/B978-0-12-821205-9.00016-2

[3] P. W. Cleary, *Particuology* **2010**, *8 (2)*, 106–118. DOI: https://doi.org/10.1016/j.partic.2009.05.006

[4] W. R. Ketterhagen, J. S. Curtis, C. R. Wassgren, B. C. Hancock, *Powder Technol.* **2009**, *195 (1)*, 1–10. DOI: https://doi.org/10.1016/j.powtec.2009.05.002

[5] B. Blais, D. Vidal, F. Bertrand, G. S. Patience, J. Chaouki, *Can. J. Chem. Eng.* **2019**, *97 (7)*, 1964–1973. DOI: https://doi.org/10.1002/cjce.23501

[6] A. A. Munjiza, *The Combined Finite-Discrete Element Method*, Wiley, London, **2004**.

[7] W. Leclerc, H. Haddad, M. Guessasma, *Int. J. Solids Struct.* **2019**, *160*, 276–292. DOI: https://doi.org/10.1016/j.ijsolstr.2018.10.030

[8] W. Zhong, A. Yu, X. Liu, Z. Tong, H. Zhang, *Powder Technol.* **2016**, *302*, 108–152. DOI: https://doi.org/10.1016/j.powtec.2016.07.010

[9] J. Qiao, P. Wen, C. Duan, W. Wang, *Adv. Powder Technol.* **2020**, *31 (3)*, 1181–1195. DOI: https://doi.org/10.1016/j.apt.2019.12.036

[10] Z. Hu, H. Zeng, Y. Ge, W. Wang, J. Wang, *Processes* **2021**, *9 (7)*, 1239. DOI: https://doi.org/10.3390/pr9071239

[11] S. P. Gundupalli, S. Hait, A. Thakur, *Waste Manage.* **2017**, *60*, 56–74. DOI: https://doi.org/10.1016/j.wasman.2016.09.015

[12] R. C. Bruce, P. Lestringant, C. A. Brenneman, H. Heymann, A. Oberholster, *Foods* **2021**, *10 (2)*, 402. DOI: https://doi.org/10.3390/foods10020402

[13] L. A. Paluchowski, E. Misimi, L. Grimsmo, L. L. Randeberg, *Food Control* **2016**, *62*, 337–345. DOI: https://doi.org/10.1016/j.foodcont.2015.11.004

[14] R. P. Haff, T. C. Pearson, E. Maghirang, *Food Measure* **2013**, *7 (4)*, 149–157. DOI: https://doi.org/10.1007/s11694-013-9150-7

[15] C. Robben, H. Wotruba, *Minerals* **2019**, *9 (9)*, 523. DOI: https://doi.org/10.3390/min9090523

[16] E. Gülcan, Ö. Y. Gülsoy, *Int. J. Miner. Process.* **2017**, *169*, 129–141. DOI: https://doi.org/10.1016/j.minpro.2017.11.007

[17] M. Kern, L. Tusa, T. Leißner, K. G. van den Boogaart, J. Gutzmer, *J. Cleaner Prod.* **2019**, *234*, 1144–1152. DOI: https://doi.org/10.1016/j.jclepro.2019.06.259

[18] C. Hoffmann Sampaio et al., *Minerals* **2021**, *11 (8)*, 904. DOI: https://doi.org/10.3390/min11080904

[19] F. Hollstein, I. Cacho, S. Arnaiz, M. Wohllebe, in *Proc. of Advanced Environmental, Chemical, and Biological Sensing Technologies XIII*, Baltimore, Maryland, United States, **2016**, 98620J. DOI: https://doi.org/10.1117/12.2220769

[20] R. D. Pascoe, R. Fitzpatrick, J. R. Garratt, *Miner. Eng.* **2015**, *72*, 101–107. DOI: https://doi.org/10.1016/j.mineng.2014.12.026

[21] R. S. Fitzpatrick, H. J. Glass, R. D. Pascoe, *Miner. Eng.* **2015**, *79*, 176–184. DOI: https://doi.org/10.1016/j.mineng.2015.06.009

[22] C. Pieper et al., *Powder Technol.* **2016**, *301*, 805–814. DOI: https://doi.org/10.1016/j.powtec.2016.07.018

[23] C. Pieper et al., *Powder Technol.* **2018**, *340*, 181–193. DOI: https://doi.org/10.1016/j.powtec.2018.09.003

[24] J. Ai, J.-F. Chen, J. M. Rotter, J. Y. Ooi, *Powder Technology* **2011**, *206 (3)*, 269–282. DOI: https://doi.org/10.1016/j.powtec.2010.09.030

[25] R. Di Felice, *Int. J. Multiphase Flow* **1994**, *20 (1)*, 153–159. DOI: https://doi.org/10.1016/0301-9322(94)90011-6

[26] A. Hölzer, M. Sommerfeld, *Powder Technol.* **2008**, *184 (3)*, 361–365. DOI: https://doi.org/10.1016/j.powtec.2007.08.021

[27] D. C. Wilcox,, *Turbulence Modeling for CFD*, 3rd ed., DCW Industries, La Canada, CA **2006**.

[28] F. Elskamp, H. Kruggel-Emden, M. Hennig, U. Teipel, *Granular Matter* **2017**, *19 (3)*, 46. DOI: https://doi.org/10.1007/s10035-017-0710-0

[29] B. Picinbono, *IEEE Trans. Signal Processing* **1997**, 552–560. DOI: https://doi.org/10.1109/78.558469